Petroleum Science 23 (2026) 3906–3919

Contents lists available at ScienceDirect

Petroleum Science

journal homepage: www.keaipublishing.com/en/journals/petroleum-science

Original Paper

Application of 2D full-waveform inversion for characterizing potential gas reservoirs

Kai Ren [a,b], Shao-Ping Lu [a,b,*], Xin-Tong Dong [c], Xiang Li [d], Xiao Ge [e], Shu-Kui Zhang [f]

[a] School of Earth Sciences and Engineering, Sun Yat-Sen University, Zhuhai, 519000, Guangdong, China
[b] Southern Marine Science and Engineering Guangdong Laboratory (Zhuhai), Zhuhai, 519000, Guangdong, China
[c] College of Instrumentation and Electrical Engineering, Jilin University, Changchun, 130000, Jilin, China
[d] CNPC Bureau of Geophysical Prospecting Inc., CNPC, Zhuozhou, 072750, Hebei, China
[e] Interdisciplinary Center, Shandong University, Jinan, 250000, Shandong, China
[f] School of Future Technology, Shandong University, Jinan, 250000, Shandong, China

A R T I C L E I N F O

Article history:
Received 2 July 2025
Received in revised form
26 December 2025
Accepted 16 March 2026
Available online 19 March 2026

Edited by Meng-Jiao Zhou

Keywords:
Full waveform inversion
Reservoir characterizing
AVA analysis

A B S T R A C T

The application of full waveform inversion (FWI) on field data is currently a widely concerned challenge in seismic exploration. FWI has been proven on synthetic data to have the ability to obtain high-accuracy subsurface velocity and improve the imaging effect of the pre-stack depth migration (PSDM). However, its practical application remains constrained by challenges such as cycle-skipping. Meanwhile, the method's capability to recover detailed subsurface properties retains considerable, yet underexploited, potential for advanced geological interpretation. In this study, we integrated FWI with amplitude variation with angle (AVA) analysis to identify potential gas reservoirs using 2D OBC data from the South China Sea. Our workflow began with 0–9 Hz FWI processing to obtain an updated velocity model. Comparative analysis demonstrated the FWI model's superiority over the initial model through: (1) improved data fitting, (2) enhanced PSDM imaging with better structural alignment, and (3) higher-quality ADCIGs. The FWI results revealed a distinct high-velocity anomaly, which was validated through integration with PSDM images and well data. Subsequent AVA analysis suggested this anomaly may represent gas-bearing sandstone, though additional verification would be required to fully characterize the formation. Nonetheless, our workflow offers a reference for subsequent interpretations, which narrows down the scope for targeted objects. Our findings demonstrate that FWI and ADCIGs can obtain more geological information than traditional velocity modeling methods, thereby becoming a valuable tool for geological interpretation.

1. Introduction

The South China Sea is regarded as China's principal area for offshore oil and gas reserves (Xu et al., 2012). A number of oil and gas reservoirs in this area are associated with deep-seated faults (Zhou et al., 2019; Gao et al., 2020). These faults serve not only as conduits for hydrocarbon migration but are also crucial for forming reservoir traps where oil and gas accumulate, which are considered favorable accumulation zones for oil and gas reservoirs (Li et al., 2012). Consequently, the precise localization and extraction of subsurface oil reserves, particularly oil resources at greater depths, require accurate imaging of subsurface fault structures. This is only a preliminary interpretation that requires further analysis to determine the specific attributes of the stratum.

Nevertheless, accurately imaging deep fault structures is still challenging in seismic exploration. The most common and convincing tool of subsurface imaging is pre-stack depth migration (PSDM) (Deng and McMechan, 2007). PSDM can obtain migration images that reflect the real position of subsurface structures. Based on different principles, several methods were developed to realize

* Corresponding author.
E-mail address: lushaoping@mail.sysu.edu.cn (S.-P. Lu).
Peer review under the responsibility of China University of Petroleum (Beijing).

https://doi.org/10.1016/j.petsci.2026.03.034
1995-8226/

PSDM, such as Kirchhoff migration (Buske, 1999), reverse time migration (RTM) (Baysal et al., 1983; McMechan, 1983), one-way wave equation migration (WEM) (Zhang et al., 2005) and least-squares migration (LSM) (Nemeth et al., 1999). These imaging methods can obtain detailed images of subsurface structures and have been successfully applied in industry (Cabrera et al., 1992; Shin et al., 2001).

Although detailed subsurface structures can be revealed by migration, it is still difficult to figure out the underground reservoirs on the PSDM image. The PSDM image can reveal the structure or reflection coefficient of the underground strata (Nemeth et al., 1999), and can reveal the geological properties from further AVA analysis, which is important to figure out reservoirs. Besides, more physical property information on subsurface structures can also aid in geological interpretation, such as subsurface velocity, well logging data, and other geological information. In particular, the velocity of subsurface media contains geological information, and the lithology of subsurface structure can be estimated if the subsurface velocity model is accurate. Besides, the accuracy of the PSDM image also relies on the accuracy of the subsurface velocity model, and an inaccurate subsurface velocity will lead to incorrect structures in the PSDM image (Versteeg, 1993), which will interfere with the results of geological interpretation. These factors make it crucial to obtain an accurate subsurface velocity model.

In seismic data processing, many methods have been used to build subsurface velocity models for pre-stack migration, such as migration velocity analysis (MVA) (Chauris et al., 2002; Fei and McMechan, 2006) or travel time tomography (Bording et al., 1987; Zhou et al., 2016; Yang et al., 2021) and full-waveform inversion (FWI) (Tarantola, 1984). The MVA method and travel time tomography method are widely used in geophysics to reconstruct the subsurface velocity structure (Zhu et al., 2000; Taillandier et al., 2009; Yang et al., 2021). However, these methods are difficult to apply to fault areas. Usually, the subsurface velocity of the fault area changes drastically in both horizontal and vertical directions. The low-frequency background velocity field estimated by MVA or travel time tomography cannot capture these dramatic changes, making it difficult to apply this method to fault areas (Yang and Zhang, 2019).

Full-waveform inversion (FWI) is a velocity-building method proposed in the 1980s (Tarantola, 1984; Gauthier et al., 1986; Mora, 1987). The objective of FWI is to build a high-resolution subsurface velocity model, and this method can automatically update the velocity model by matching the waveform record of observed and synthetically modelled data. Compared with travel time tomography, FWI can reconstruct more high-resolution and high-fidelity velocity models (Warner et al., 2013).

Although FWI is theoretically more accurate, it still needs to be improved in field data application. The forward and inversion in FWI are strong nonlinear problems, resulting in relatively harsh application conditions for FWI. FWI can be applied in acoustic or elastic wave media (Warner et al., 2013) and can estimate subsurface velocity models using full waveform information or partial waveform information, such as reflected waves (Xu et al., 2012). These FWI approaches require solving a nonlinear inversion problem, and the global optimization algorithms required to solve this problem are computationally expensive. A practical alternative is to use local optimization algorithms starting with a sufficiently accurate initial velocity model, this approach can mitigate the non-linearity of the inversion problem, instead of solving nonlinear problems directly (Li et al., 2016), which has also made FWI obtain some good results in synthetic data (Lee and Kim, 2003; Hu et al., 2009).

Although the local optimization method can avoid directly solving the nonlinear FWI problem and obtain accurate results when the initial model is good enough, it is still challenging to apply FWI to field data. The local optimization method may fall into a local minimum when the initial model is not accurate enough, especially when the low-frequency information is not available in the field data.Métivier et al. (2018) and Pladys et al. (2021) optimized the objective function to avoid cycle-skipping. To improve the applicability of FWI, several inversion strategies are applied to improve the accuracy of FWI results (Warner and Guasch, 2016; Davy et al., 2018; Borisov et al., 2020). First, a better starting model is obtained to make sure the model is close enough to the true model. Second, the FWI iterations are performed step by step from the low-frequency band to the high-frequency band using a multiscale inversion strategy (Bunks et al., 1995; Wang et al., 2019; Huang et al., 2021). During each band, the velocity model is updated gradually to match the observed data and forward modeling data from long-wavelength to short-wavelength.

After optimizing the inversion process through updates in algorithms and strategies, FWI has been applied to streamer seismic data and ocean-bottom cable (OBC) and has gotten reliable results in recent years. Sirgue et al. (2010) used this method to a 3D OBC dataset at Valhall in the North Sea. They obtained a high-accurate velocity model, which improved the PSDM image and revealed many geological features. Dickinson et al. (2017) obtained a reliable FWI result at North West Shelf offshore Australia by using a layer-stripping scheme. Jamali Hondori et al. (2021) used the migration velocity analysis method to build an accurate initial model and applied FWI to limited-offset marine streamer seismic data at the Japan Trench Forearc Slope. These application cases proved that accurate FWI results can help subsurface imaging and can also help reveal hidden geological details.

With the progress of FWI application, the ADCIGs can be calculated during migration processing. In addition to reflecting the velocity accuracy, ADCIGs also contains the amplitude variation with angle information (Wang et al., 2014). The AVA curve of a formation with specific properties can be obtained through theoretical calculation. By comparing the AVA curve of actual data with the theoretical AVA curve, its possible formation properties can be inferred (Wang et al., 2005).

The accuracy of ADCIGs is crucial for AVA analysis, which is dependent on the precision of the velocity model and the algorithms employed to compute ADCIGs. Two main primary algorithms, the subsurface offset-to-angle (Sava and Fomel, 2003) and directional vector (Yoon and Marfurt, 2006) methods, are widely used in computing ADCIGs and can obtain convincing results when the subsurface velocity is locally smooth. However, when the subsurface structure is complex, the subsurface offset-to-angle method may provide low-accuracy subsurface reflection angles, and the directional vector method may provide a result with crosstalk noise. To generate accurate ADCIGs, Zhang et al. (2022, 2023, and 2024) proposed a series of algorithms on computing ADCIGs based on the Poynting vector. A Hilbert transform to the wavefields is added to the algorithm to calculate the stabilized Poynting vector, which is more stable and accurate.

In this paper, we utilized FWI and AVA analysis to infer potential gas reservoir locations during seismic data processing on a 2D OBC dataset from the South China Sea. We first apply FWI on the field data to establish a subsurface velocity model in this area, and a potential reservoir is inferred by integrating the petrophysical information provided by the velocity model with the structural information provided by PSDM. In this survey area, large faults are cutting through the sedimentary rock basement and complex shallow stratigraphic structures subsurface, which makes the FWI in this area representative.

This paper presents a case study on the application of FWI. A high-accuracy subsurface velocity model is obtained through FWI, and a jointly interpretation is applied based on the velocity, PSDM profile and ADCIGs. This workflow successfully reveals subsurface velocity anomalies, and further interpretation reveals that the anomalies have a potential to be a gas bearing reservoir. A series of quality control measures support the reliability of these results. Although further geological interpretation is required to determine the exact attribute of the reservoir, our work provides a preliminary geological explanation and enhances the efficiency of the interpretation process.

This paper will be organized as follows. The principles of the FWI will be introduced in the Method section. We then present a specific introduction to this field data example. Because the inverted field dataset is a single OBC line, we limit our implementation to a 2D geometry. The setup of the initial model and inversion process will be discussed in detail. A subsurface velocity model in this area was obtained by applying FWI to this dataset. A series of migration results and comparisons with velocity models demonstrate the accuracy of the velocity model acquired by FWI. Based on the FWI inverted velocity, the ADCIGs were calculated, and then an AVA analysis was applied to the field data. Finally, we summarize the obtained results and discuss perspectives.

2. Method

2.1. Full waveform inversion

The nonlinear FWI can be considered as an unconstrained least squares problem:

$$\min_{m} \Phi(\mathbf{m}) = \left\{ \frac{1}{2} \|\mathbf{d} - \mathscr{F}[\mathbf{m}, \mathbf{s}]\|_2^2 \right\}, \tag{1}$$

where $\mathbf{d}$ represents the observed data that FWI needs to fit with the forward modeling operator $\mathscr{F}$, $\mathbf{m}$ represents the discrete model and $\mathbf{s}$ represents the source function. After obtaining the source function and initial model, the velocity model can be updated iteratively from a starting model $\mathbf{m}_0$:

$$\mathbf{m}_{n+1} = \mathbf{m}_n + \alpha_n \delta \mathbf{m}_n, \tag{2}$$

where $\mathbf{m}_{n+1}$ represents the $(n+1)$th updated model, α represents the velocity update step length of nth iterate calculated by line search methods, $\delta\mathbf{m}$ represents the velocity perturbation, which is the negative gradient of Eq. (1). The starting model $\mathbf{m}_0$ is assumed to be close enough to the true model. If the velocity model is updated correctly, the misfit function in Eq. (1) will decrease. The residual data of the nth iteration $\delta\mathbf{d}_n$ is defined to be the difference between the modelled and observed data, and it is clear that $\delta\mathbf{d}_n$ is related to the inverted model $\mathbf{m}_n$. The iteration problem has now become to obtain the gradient $\delta\mathbf{m}_n$ from the previous model $\mathbf{m}_n$, then the new model can be updated by Eq. (2).

The velocity perturbation $\delta\mathbf{m}$ can be calculated using local optimization algorithms, but most of these algorithms need to calculate the Hessian matrix, and the computation of the Hessian matrix will be expensive. To avoid the expensive cost of computing the Hessian matrix, the preconditioned velocity perturbation $\delta\mathbf{m}_n$ of nth iteration can be obtained using the Gauss-Newton method by solving the following linear least squares problem (Nocedal and Wright, 2006; Li et al., 2022):

$$\delta\mathbf{m}_n = \arg\min_{\delta\mathbf{m}} \|\delta\mathbf{d}_n - \nabla\mathscr{F}[\mathbf{m}_n]\delta\mathbf{m}\|_2^2, \tag{3}$$

where $\nabla\mathscr{F}[\mathbf{m}_n]$ represents the Jacobian of the nth iteration, $\delta\mathbf{d}_n$ represents the data residual between observed data $\mathbf{d}$ and forward modeling data $\mathscr{F}[\mathbf{m}_n]$ of $\mathbf{m}_n$. The FWI iteration will be repeated until the $\ell 2$ -norm of data residual $\|\mathbf{d} - \mathscr{F}[\mathbf{m}]\|_2$ is small enough.

Eqs. (1)–(3) show the process of FWI iteration. To apply this inversion process to a field dataset, a computational implementation of this process is needed. In this paper, we used a frequency-domain inversion method of Brossier et al. (2009). This iteration process includes forward modeling in the frequency domain for each source within the initial model to generate a synthetically modelled dataset. During the forward modeling and following gradients calculating, an irregular grid (Moczo, 1989) is applied to make the FWI processing more efficient. Then, the data residual is computed by subtracting the modelled and observed data trace-by-trace, a time-dependent gaining is applied to the field data to compensate the realistic variation of amplitude with offset, and the contribution to the gradient from each source is then calculated from the residual data. These gradients are then stacked to form a global gradient, which is mentioned in Eq. (3). After the calculation of the gradient, a linear search method is used to find the best step length, which makes the misfit function converge the fastest. Two strategies for determining the termination of iteration are applied to the inversion: when the step length is less than a certain threshold for multiple consecutive iterations, or when the number of inversion iterations reaches the maximum set value, the inversion iteration terminates.

Except for the computational implementation of FWI, some information is also needed for the FWI process. As discussed above, a best-guessed initial model and a source wavelet are also needed as input. The accuracy of the initial model and source wavelet is very important to FWI. When the initial input to the inversion is not accurate enough and lacks low-frequency components, the inversion will cause cycle skipping, finally leading to an inaccurate inversion result. The inverted model will not be good enough or worse than the initial model when cycle skipping occurs, but the misfit function will converge normally. An unreliable source wavelet will lead to wrong forward modeling result, which will finally cause the misfit function to not converge. Thus, an effective FWI requires quality control methods to ensure that the inversion proceeds toward the global minimum.

2.2. Data acquisition

Ocean bottom cable (OBC) is a special receiver cable that is deployed on the ocean bottom and is widely used for wide-azimuth seismic exploration to obtain large-angle waveform information. Since OBC data has a good illumination range and can obtain wide-

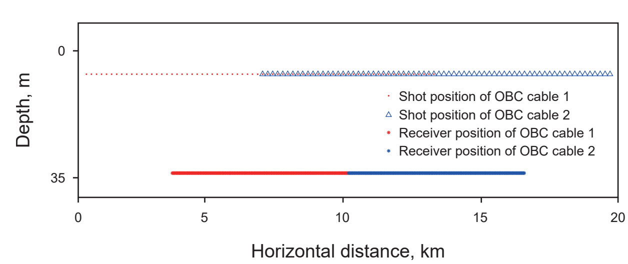

Fig. 1. Geometry of the field data. The shot points are plotted on top and the receiver points are plotted on the bottom. The shot points and OBC cable of Survey 1 is plotted in red and Survey 2 in blue. The distance between shot points is 200 m, and the distance between receiver points is 25 m.

angle information, a series of OBC seismic data acquisitions were performed to explore this fault area in the South China Sea.

The dataset used for FWI is one of the 2D datasets collected in this area. OBC surveys were deployed perpendicular to the important fault zones in the area to reveal structural details between the fault zones. This dataset contains two OBC cables and the geometry is shown in Fig. 1. Each OBC cable has 140 nodes, and the distance between nodes is 25 m. Each survey line has 70 shots, and the shot points are spaced 200 m apart. The total length of the shot line is about 20 km, and the max offset of each OBC cable is about 13 km, which is long enough to detect deep structural information.

Our workflow of data preprocessing followed by FWI is shown in Fig. 2. The data preprocessing part includes observed data denoising, wavelet estimation, and initial model building. The principal objective of denoising observed data is to enhance the signal-to-noise ratio while preserving maximal low-frequency information. Then a wavelet is obtained from denoised observed data, which is unaffected by noise, including surface waves and ghost waves. The initial model of FWI in this paper is built by the traditional travel time tomography method (Taillandier et al., 2009). After all preprocessing steps are completed, the FWI processing can be applied to the field data as described previously.

2.2.1. Data processing

Since the OBC was well coupled to the seafloor, a strong surface wave overlapped with reflection in near-offset traces, which makes it difficult to obtain a seismic wavelet. Besides, the water depth of this area is about 30 to 40 m. The shallow water environment in this area also caused the data to contain receiver ghost waves and complex multiple reflections. Moreover, linear noise and random noise were also recorded in the raw dataset.

To make the data more suitable for FWI and migration imaging, processing steps were applied to the dataset to remove the influence of linear and random noises, including *f*–*k* domain slope filtering and frequency domain random noise attenuation (RNA). Multiples and ghost waves in the data are not removed, a free surface boundary condition was applied on top of the model to simulate these waves. Furthermore, while surface waves are typically regarded as noise, they are not removed via high-pass filtering techniques during data processing to avoid the loss of low-frequency information, which may be adversely affected during filtering. Instead, these traces containing strong surface waves were excluded from the inversion to avoid the influence of surface waves. Fig. 3 shows a single shot field records at shot 70 before and after preprocessing. The records after processing look much better prepared for FWI purposes.

2.2.2. Wavelet estimating

As mentioned above, the correct wavelet is another critical factor affecting the accuracy of FWI. Wrong wavelets make it impossible to fit the observed data, eventually leading to an unconverging inversion. The acquisition of wavelets in this OBC dataset is interfered by surface waves and ghost waves. In our processing, the wavelet is first roughly calculated by stacking near offset traces after excluding traces containing surface wave to avoid the interference of surface wave. The S/N ratio is also increased after stack processing, but this wavelet still contains ghost waves. Since the influence of ghost waves on wavelets is mainly reflected in the tailing after the wave peak and the wavelets are assumed to be symmetrical, we use peak of the wavelet as mirror axis to fold the first part of the wavelet after the peak in a mirror style.

However, assuming that the wavelet is symmetric is idealistic for field data. This assumption may introduce inaccuracies in the

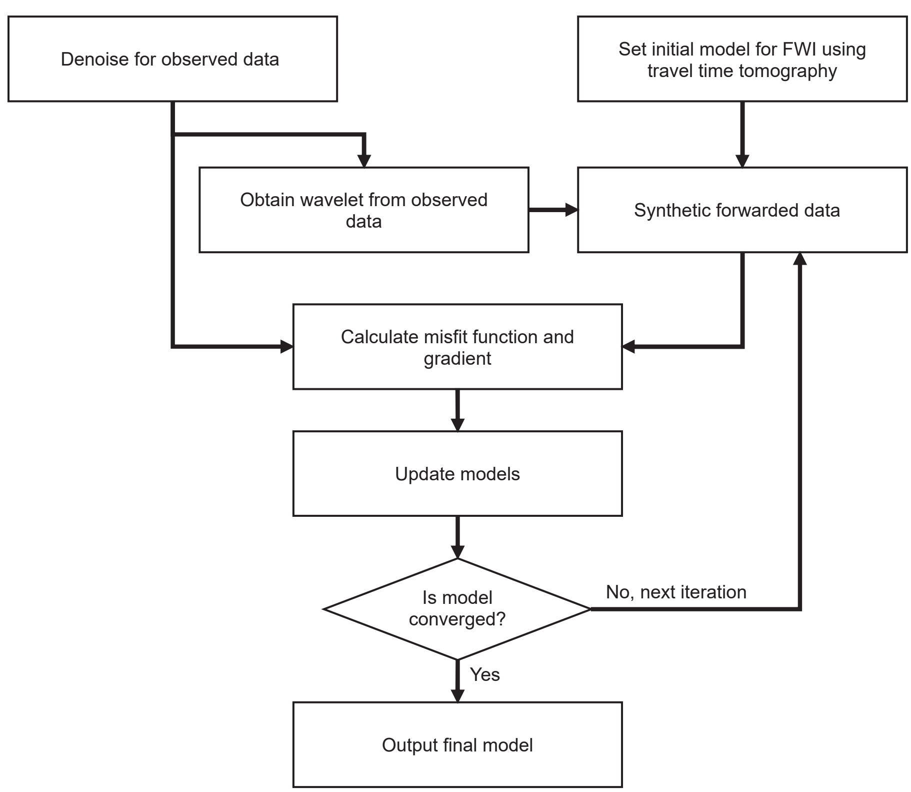

Fig. 2. Workflow for data preprocessing and FWI. Denoising process is applied to the observed data to make the data more suitable for wavelet obtaining and FWI. The initial model for FWI is built by traditional travel time tomography. Then the FWI is applied to calculate residuals between synthetically modelled data and observed data and update the model iteratively.

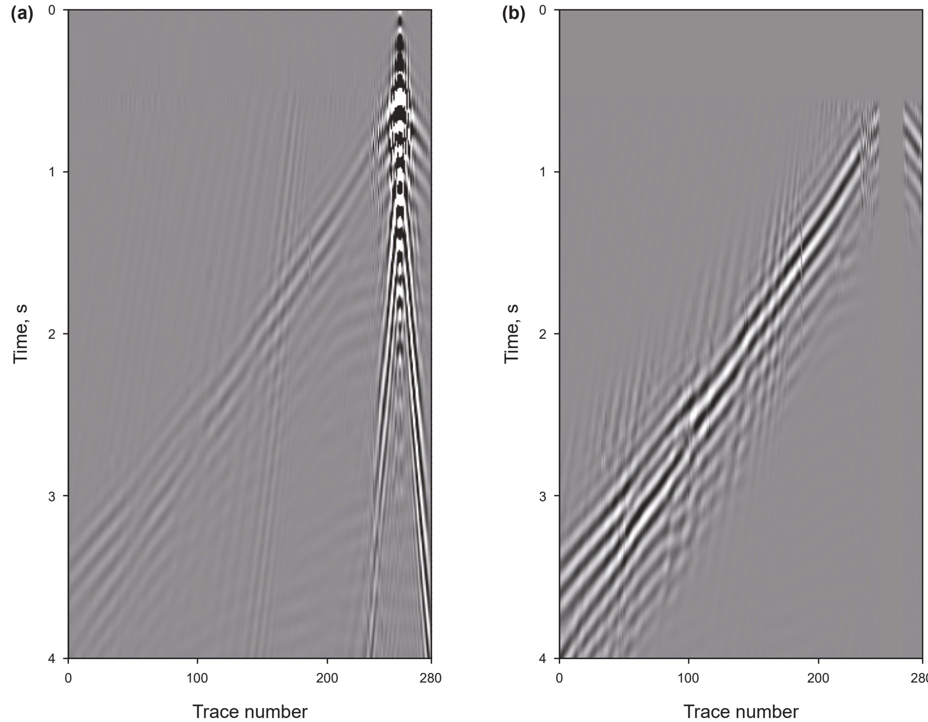

Fig. 3. (**a**) Raw and (**b**) denoised field data at shot 70. The surface wave and other noise are removed after processing, and the refraction wave used for FWI is enhanced. The S/N ratio is also improved after processing.

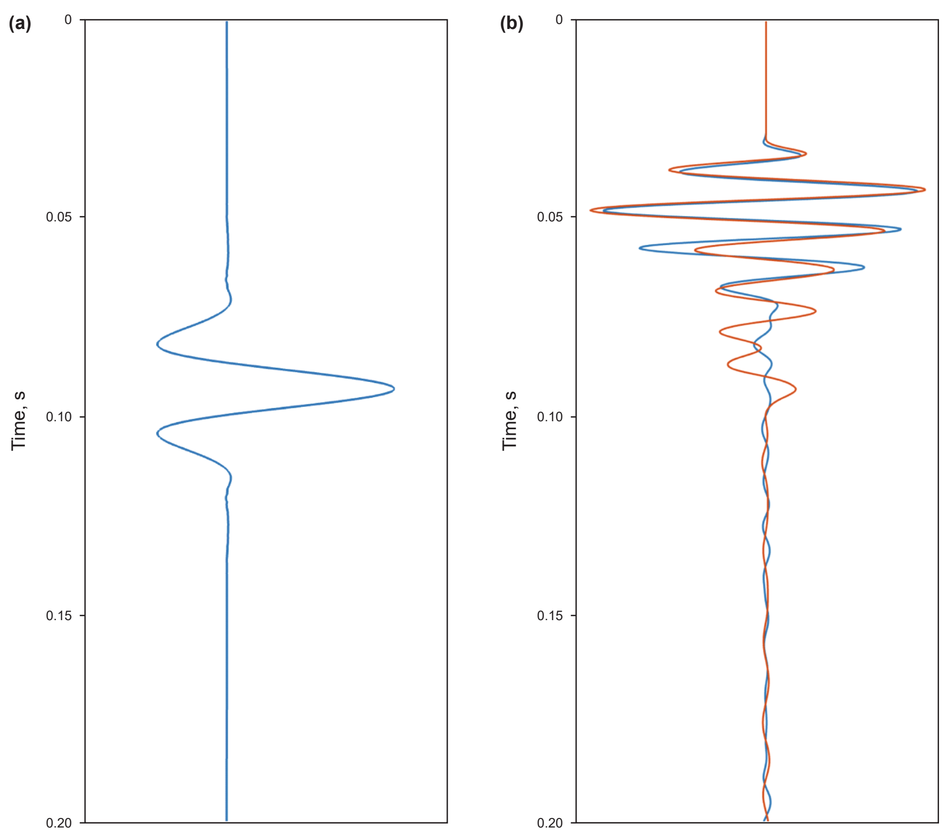

Fig. 4. Wavelet and the fitness comparison of field and synthetically modelled data at near offset. (**a**) Estimated wavelet at 0–9 Hz frequency band, (**b**) fitness comparison of field and synthetically data modelled by wavelet in (a) at near offset (200 m), blue line represents the synthetically modelled data and red line represents the field data.

wavelet, which could further affect the inversion results. Therefore, a quality control process is conducted by comparing the field data with the synthetically modelled data generated by the estimated wavelet. A high-accuracy wavelet will produce a similar waveform to the field data. Fig. 4 shows the estimated wavelet and the match effect between the synthetic data and the field data waveform at an offset of 200 m. It can be seen that the field data fit well with the synthetically modelled data, which proves that the obtained seismic wavelet is reliable.

2.2.3. Initial model

Based on the dataset after processing, an initial model was developed using traditional first arrival time tomography. The first arrival time was picked manually, and the initial model of FWI was built by fitting the picked travel time and travel time calculated by solving the Eikonal equation. Due to the sparse shot points, a smooth factor was applied to the velocity model to mitigate the influence of the ray path. The initial model shown in Fig. 5(a) is smooth, with a low-velocity layer at a depth of 3 km to 4 km, and shows the general structure of the subsurface in this area. However, the details of the low-velocity layer top interface, deep faults, and shallow sedimentary layers are still lacking. Therefore, the purpose of FWI is to obtain a higher-resolution velocity model to reveal these subsurface structures.

2.3. ADCIGs calculating

After a high accurate velocity model is inverted by FWI, the angle domain common imaging gathers (ADCIGs) can be calculated during the PSDM processing. The ADCIGs can not only evaluate the accuracy of the velocity model but also proposed as a technique for validating seismic amplitude anomalies when the wavefield direction and amplitude relationship is calculated correctly. In our PSDM processing, we used a true-amplitude one-way wave equation migration (WEM) (Lu, 2021; Zhang et al., 2005) with a deconvolution imaging condition (Lu, 2021; Guitton et al., 2007) to generate a PSDM image, which can ensure the true amplitude relationship is preserved. Additionally, the ADCIGs were calculated using a stabilized Poynting vector method, which has been proven accurate and efficient in calculating imaging angles. A coverage correction is also applied when calculating ADCIGs to eliminate the effect of footprints.

The deconvolution imaging condition is as follows:

$$\mathbf{I}_{\text{ADCIGs}}(\mathbf{x},\theta_n)=\int_0^{T_{\max}}\frac{\mathbf{u}_{\text{s}}^{\text{down}}(\mathbf{x};t)\cdot\mathbf{u}_{\text{r}}^{\text{up}}(\mathbf{x};T_{\max}-t)}{\mathbf{u}_{\text{s}}^{\text{down}}(\mathbf{x};t)\cdot\mathbf{u}_{\text{s}}^{\text{down}}(\mathbf{x};t)}\delta(\theta-\theta_n)\text{d}t \tag{4}$$

where $\mathbf{I}_{\text{ADCIGs}}$ represents the angle gather for PSDM imaging. $\mathbf{x}$ represents the subsurface location, $\mathbf{u}_{\text{s}}^{\text{down}}$ represents the source-side down-going wavefield and $\mathbf{u}_{\text{r}}^{\text{up}}$ represents the receiver-side up-going wavefield. θ_n represents the binning angles in the imaging processing, which is calculated using

$$\theta_n=\arccos\left[\frac{\left(\mathbf{p}_{\text{s}}^{\text{h}}\cdot\mathbf{p}_{\text{r}}^{\text{h}}\right)}{\left|\mathbf{p}_{\text{s}}^{\text{h}}\right|\left|\mathbf{p}_{\text{r}}^{\text{h}}\right|}\right]\Big/2 \tag{5}$$

where $\mathbf{p}_{\text{s}}^{\text{h}}$ and $\mathbf{p}_{\text{r}}^{\text{h}}$ represent the source-side and receiver-side stabilized Poynting vectors, respectively, and $|\cdot|$ denotes the norm of stabilized Poynting vectors. Different from the traditional Poynting vector calculation algorithm, stabilized Poynting vector is calculated as follows:

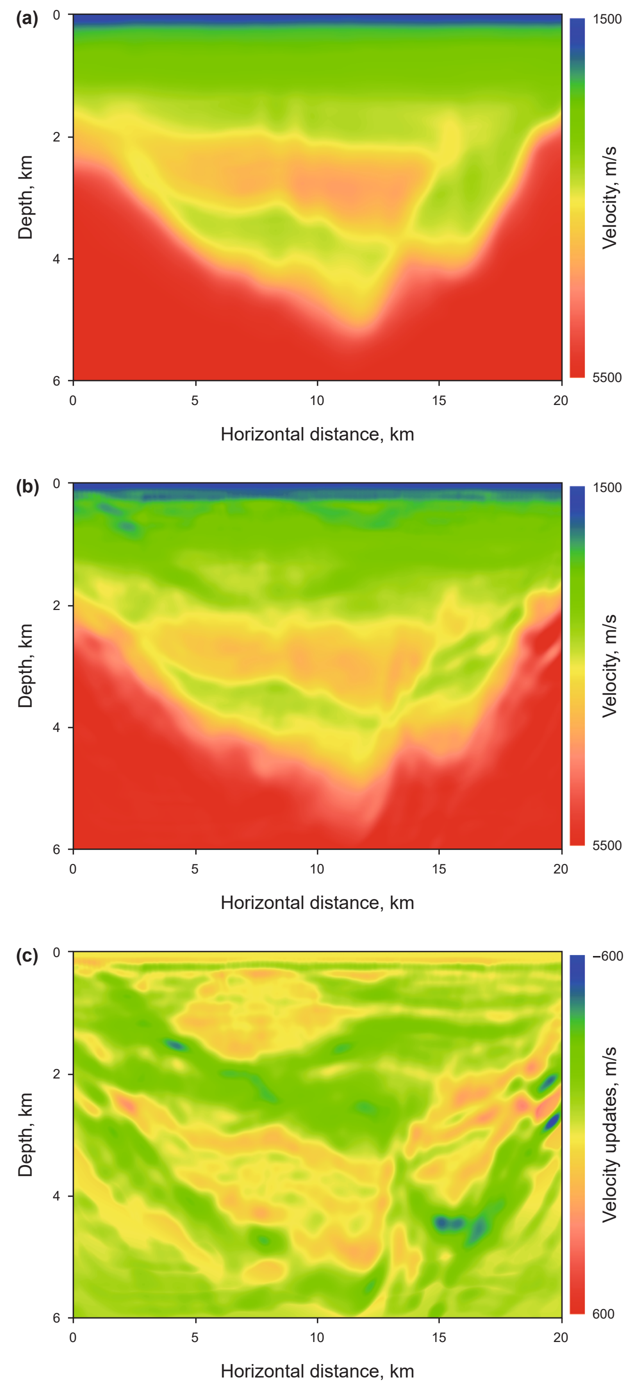

Fig. 5. **(a)** Initial model built by traditional travel time tomography, **(b)** final FWI result and **(c)** velocity update between (b) and (a). The initial model is smooth and more structures are revealed in FWI result.

$$\begin{cases}\mathbf{p}_{\text{s}}^{\text{h}}(\mathbf{x};t)=-\dfrac{\partial\mathbf{u}_{\text{s}}^{\text{down}}(\mathbf{x};t)}{\partial t}\nabla\mathbf{u}_{\text{s}}^{\text{down}}(\mathbf{x};t)-\dfrac{\partial\mathbf{u}_{\text{s}}^{\text{h,down}}(\mathbf{x};t)}{\partial t}\nabla\mathbf{u}_{\text{s}}^{\text{h,down}}(\mathbf{x};t)\\ \mathbf{p}_{\text{r}}^{\text{h}}(\mathbf{x};t)=-\dfrac{\partial\mathbf{u}_{\text{r}}^{\text{up}}(\mathbf{x};t)}{\partial t}\nabla\mathbf{u}_{\text{r}}^{\text{up}}(\mathbf{x};t)-\dfrac{\partial\mathbf{u}_{\text{r}}^{\text{h,up}}(\mathbf{x};t)}{\partial t}\nabla\mathbf{u}_{\text{r}}^{\text{h,up}}(\mathbf{x};t)\end{cases} \tag{6}$$

where $\mathbf{u}_{\text{s}}^{\text{down}}$ and $\mathbf{u}_{\text{r}}^{\text{up}}$ represent the source-side down-going and receiver-side up-going wavefields, respectively. $\mathbf{u}_{\text{s}}^{\text{h,down}}$ and $\mathbf{u}_{\text{r}}^{\text{h,up}}$

represent the wavefields with the Hilbert transform along the time axis corresponding to $\mathbf{u}_s^{down}$ and $\mathbf{u}_r^{up}$. The phase of $\mathbf{u}_s^{h,down}$ and $\mathbf{u}_r^{h,up}$ is 90° shifted to the original wavefields, which resolve the instability problem induced by the oscillatory nature. Therefore, the imaging condition of angle can be calculated by combining Eqs. (4)–(6).

3. Results

As the data processing section mentioned, the minimum offset was limited to 200 m to remove surface waves. We sequentially apply FWI in a frequency band range of 0–9 Hz. Therefore, all data processing steps and wavelet generation were performed after a low-pass filter of 0–9 Hz to ensure data consistency. During the inversion process, the velocity model is gradually inverted from low frequency to high frequency. The inversion is divided into two frequency bands: 0–6 Hz and 0–9 Hz, and each band contains 40 iterations, which prevents local optimal solutions caused by different signal strengths between different frequency bands. After an inversion of 80 iterations, the final velocity model of FWI is shown in Fig. 5(b) and the velocity update between the initial and FWI inverted model is shown in Fig. 5(c). The inversion results appear to contain more detail than the initial model, and further comparisons are required to demonstrate the accuracy of the inversion results.

3.1. Data fitting comparison

To further prove the accuracy and reliability of the inverted velocity, a series of quality control comparisons are needed before and after performing migration. Usually, the criterion for judging the accuracy of FWI inversion results is whether the forward modeling data and the observation data can fit well. The most direct and convenient way is to directly compare the observed and synthetically modelled data. If the inversion is successfully performed, the forward data of the inverted model will be more similar to the observed data than the initial model.

Fig. 6 shows the comparison between the synthetically modelled data of the inverted and initial model and the observed data. Some of the refracted waves in the observed data are marked with red dots in Fig. 6(a)–(c). The forward modeling results of both the initial and final models fit well with the observational data at near offsets, proving the accuracy of the obtained wavelet. As the offset increases, the error between forward data and observation data gradually increases. At the maximum offset, the waveform details at the red dots in Fig. 6(a) do not match the observed data, while the FWI result fits well with the observed data in Fig. 6(c).

Besides, Fig. 6(d) and (e) show splicing results of modelled and observed data of the initial model and the FWI model respectively. The part with a red two-way arrow at the top of the picture represents synthetically modelled data, and the other parts are observed data. The refraction waveform information in synthetically modelled data and observed data cannot be fitted in the initial model splicing result shown in Fig. 6(d), which suggests a significant discrepancy between the initial model and the actual subsurface structure. In the FWI model splicing result shown in Fig. 6(e), the synthetically modelled data and observed data have good continuity, indicating that the data fit well between the FWI result and observed data, and proving the accuracy of the FWI inverted model.

It can be seen from the above comparison that, after FWI processing, synthetically modelled data generated from the inverted results are more similar to the observed data in both near and far offset, and the waveform details of the inverted results also match the observed data well.

3.2. Cross-correlation comparison

However, the waveform comparison cannot show the data fitting improvement trend of all traces. To directly compare the data fitting, we use cross-correlation criteria as it is a convincing method to judge the quality of data fitting. Cross-correlation describes the similarity of two waveform signals. If the inversion results can perfectly fit the observed data, the maximum lag of the cross-correlation output will be at a delayed time of 0.0. Besides, the value of the cross-correlation coefficients at maximum lag can also evaluate the data fitting, which will be 1 if the modelled data fit the observed data perfectly.

The cross-correlation of all shot between modelled and observed data of the initial model and the final inverted model is calculated trace by trace. The cross-correlation lag and coefficients comparison of initial model and FWI inverted model is shown in Fig. 7. Fig. 7(a) and (b) represents the cross-correlation lag of initial and FWI inverted model, respectively. The cross-correlation lag is arranged horizontally by shot number and vertically by traces. The maximum cross-correlation lag of a perfect data fitting result should be 0. The lag of the initial velocity model in Fig. 7(a) shows significantly larger deviations from 0, indicating that the modelled and observed data does not fit well. In contrast, the lags from the FWI inverted model in Fig. 7(b) are tightly clustered around zero, demonstrating a critical improvement in temporal alignment achieved through the FWI process. Fig. 7(c) and (d) represents the cross-correlation coefficients of initial model and FWI inverted model, respectively. It can be observed that the cross-correlation coefficients value of FWI inverted model in Fig. 7(d) show a striking increase than initial model, especially in large offset, which proves that the waveform cross-correlation after FWI processing is better and the synthetically modelled dataset of inverted data is more similar to observed data.

3.3. Migration comparison

The data fit comparisons can only show the fit improvement between the forward modeling data and the observed data. Still, they cannot directly indicate that the inverted velocity model has become more accurate. As mentioned above, the final goal of FWI is to improve the imaging fidelity in fault areas. A velocity model with better accuracy can get a better migration result. Thus, the migration imaging effect was used to judge the accuracy of the inverted model. A convincing FWI result should improve the imaging effect of the fault zone.

Therefore, pre-stack depth migration (PSDM) was performed using initial velocity and inverted velocity to compare the accuracy of the initial model and inverted model. Fig. 8 shows the PSDM result using the initial and FWI inverted models. The fault structure in the initial model result shown in Fig. 8(a) is discontinuous, and the deep fault cannot be imaged (red dotted line box), and the imaging of the intersection between strata and faults is not clear. The migration results generated using the inverted model shown in Fig. 8(b) has a better imaging effect at deep fault areas. The deep fault structure has better continuity than the initial model, and the imaging of the intersection between strata and faults is more precise. These improvements in imaging effects prove that the inversion velocity model has higher accuracy.

3.4. ADCIGs comparison

The accuracy of the velocity model can also be proven by comparing angle-domain common-image gathers (ADCIGs) based on the PSDM results. The ADCIGs can be calculated from migration

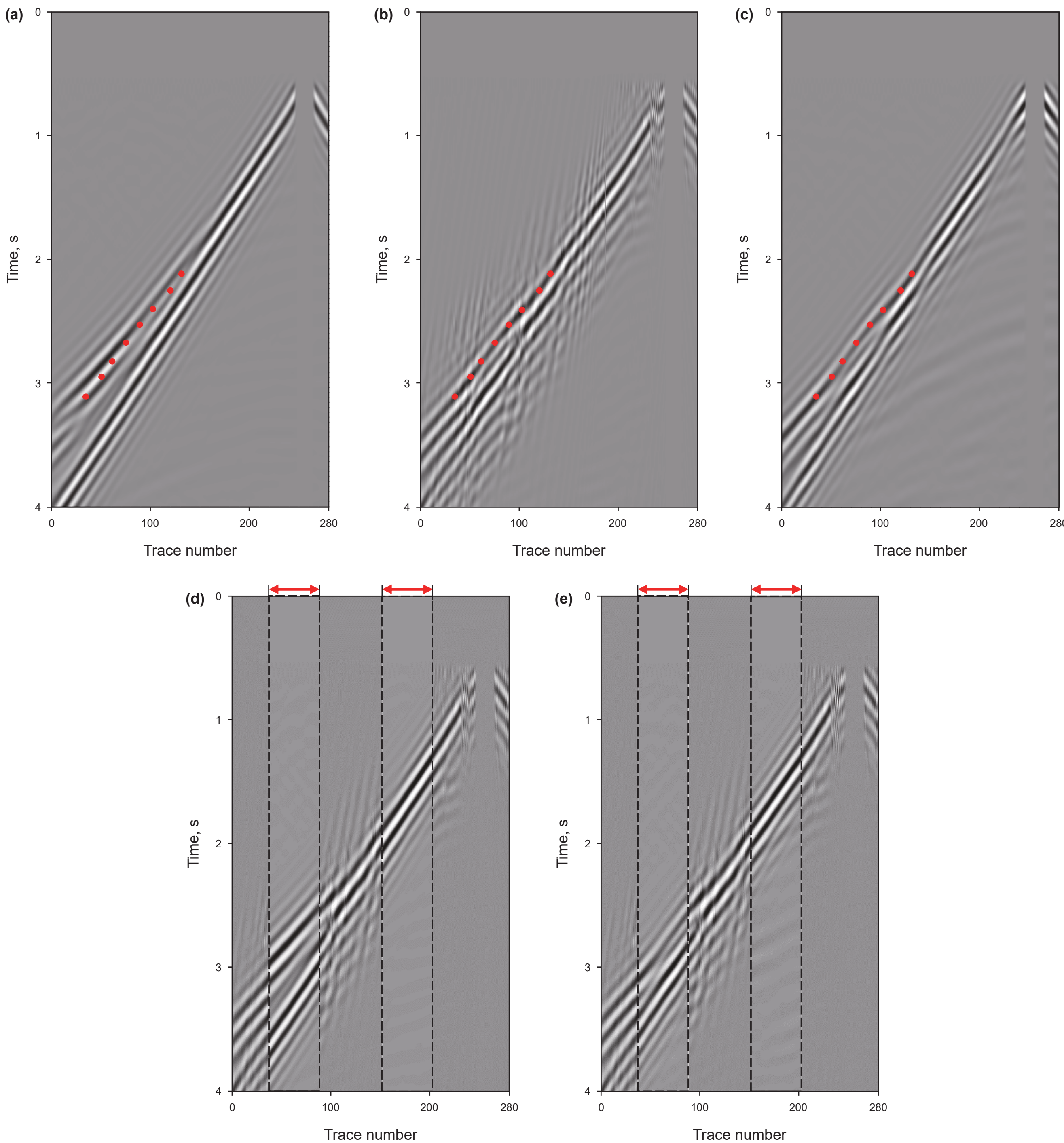

Fig. 6. Data fitting comparison between synthetically modelled data and observed data of initial model and FWI inverted model. **(a)** Synthetically modelled data of initial model, **(b)** observed data, **(c)** synthetically modelled data of FWI inverted model, red dot line marks the position of refraction wave in observed data. **(d)** Splicing result of initial model and observed data, **(e)** splicing result of FWI inverted model and observed data, synthetically modelled data is mark with a two-way arrow on the top of the figure.

results by using the Poynting vector (Zhang and Lu, 2022; Zhang et al., 2023; Zhang et al., 2024). The event in ADCIGs will be aligned horizontally along angles within a gather if the velocity model is accurate. To compare the effect of velocity model updates on the ADCIGs results, 9 ADCIGs along the PSDM image from 5 km to 13 km are extracted. Fig. 9 shows the ADCIGs using the FWI inverted model and the initial model. Due to the velocity update between the initial model and the FWI inverted model, discrepancies in the depth of the strata appear within their ADCIGs. The position of deep faults is marked by red arrows. The initial velocity model is built through first arrival time tomography methods (Taillandier et al., 2009). This approach faces challenges in obtaining short wavelength velocity perturbation, and may resulting in a velocity with less high-resolution details, which will affect the migration result, especially in fault area. Consequently, the event of the initial velocity model ADCIGs shows a more curved shape. The event of FWI results is straighter in the deep fault area, which proves that the FWI inverted model is of higher

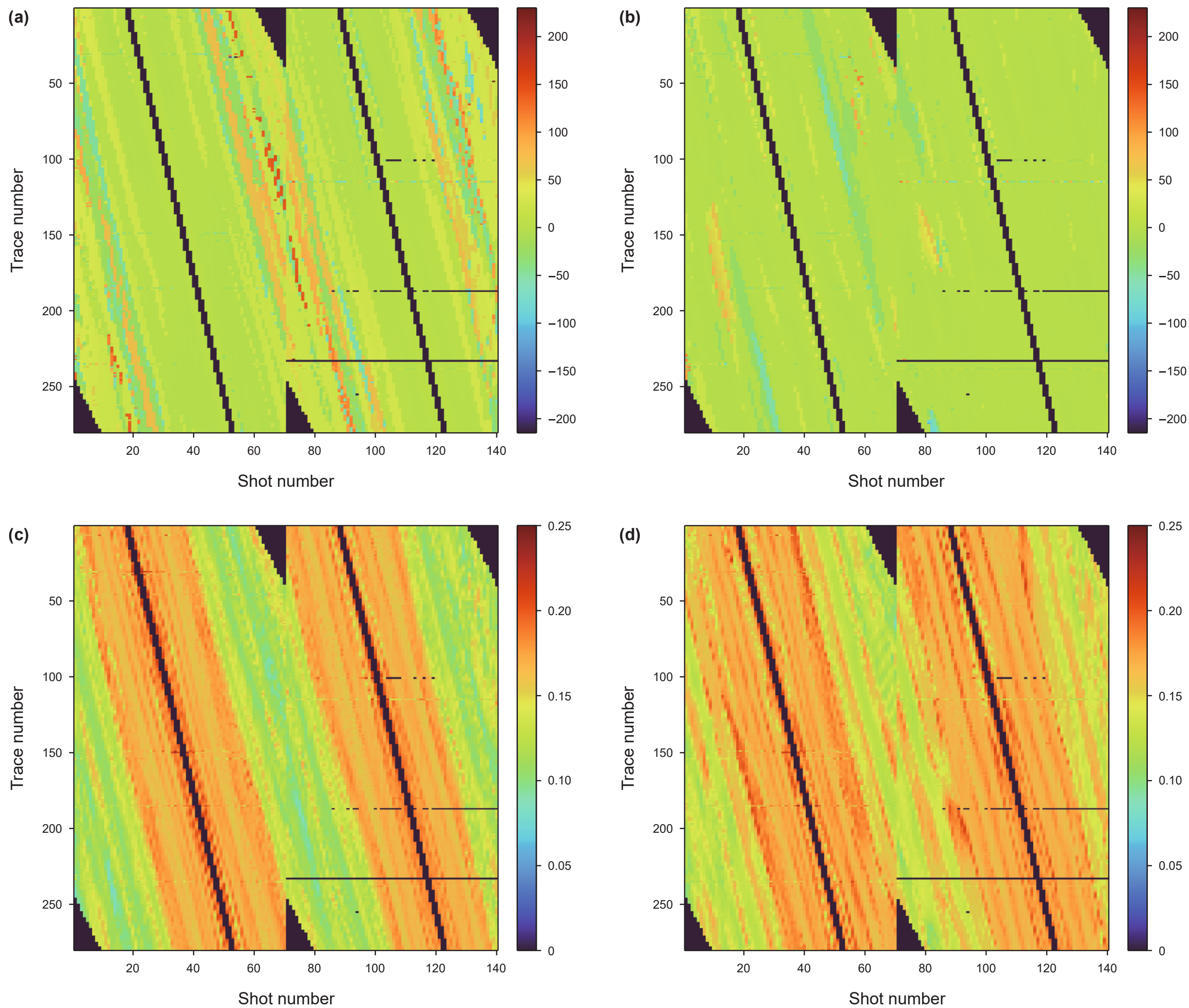

Fig. 7. Cross-correlation comparison of initial model and FWI inverted model. **(a)** Represents the lag at maximum cross-correlation of initial model; **(b)** represents the lag at maximum cross-correlation of FWI inverted model; **(c)** represents the maximum cross-correlation coefficients of initial model; **(d)** represents the maximum cross-correlation coefficients of FWI inverted model.

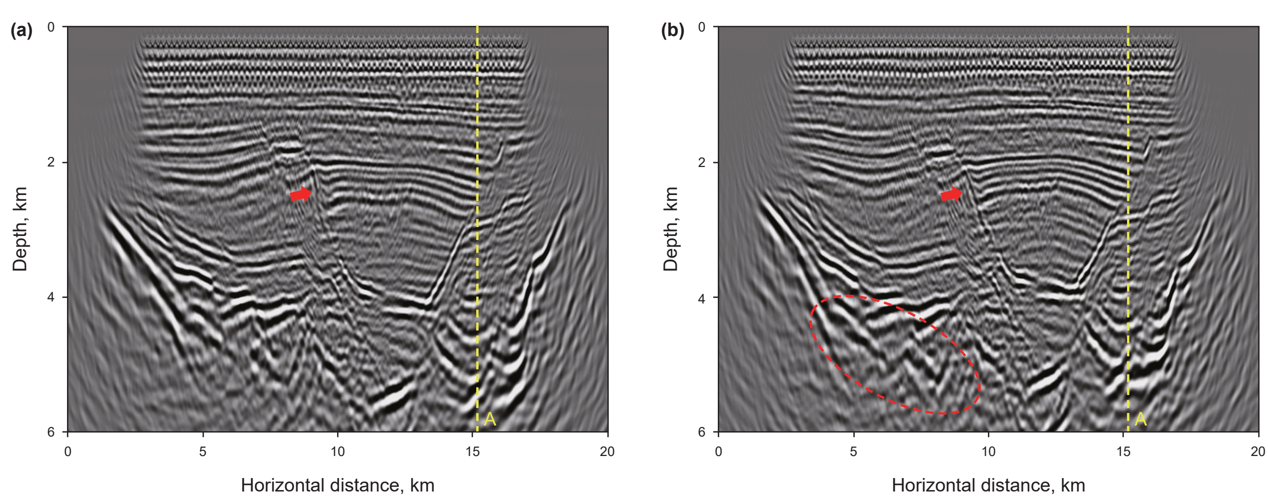

Fig. 8. PSDM image comparison of **(a)** initial model and **(b)** FWI inverted model. The deep fault zone is marked with a dotted line ellipse and the intersection between strata and faults are indicated by red arrows in (a) and (b).

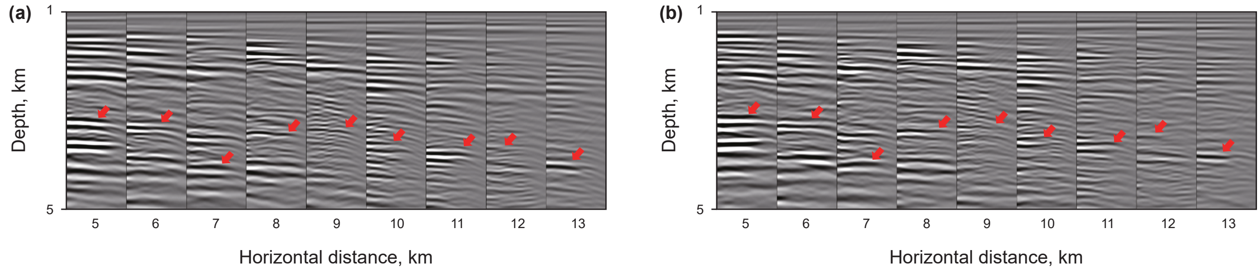

Fig. 9. ADCIGs results of **(a)** initial model and **(b)** FWI inverted model. The red arrows indicate the improvement of the FWI model on the flattening the events of ADCIGs.

accuracy. These comparative tests show that the FWI model has better accuracy and can obtain clearer and more accurate subsurface structures through migration imaging.

The aforementioned comparison has demonstrated that FWI enhances the accuracy of the inversion model. Nonetheless, a direct comparison between the inversion velocity model and the actual subsurface velocity remains absent. To further demonstrate the accuracy of the FWI result, we compare the inverted subsurface model with the acoustic well log velocity located on the right of the profile. The well velocity data is located at $x = 13.25$ km, and the data is recorded from 2.7 km to 3.3 km. The initial velocity, inverted velocity, and the well data are represented in Fig. 10. The velocity update is evident, and the FWI inverted model is consistent better with the well log's velocity, while the initial velocity model obtained from the traditional method does not match the well log velocity. Velocity anomalies are one of the indicators of oil and gas reservoirs. Therefore, it is necessary to further analyze these high-velocity anomaly areas.

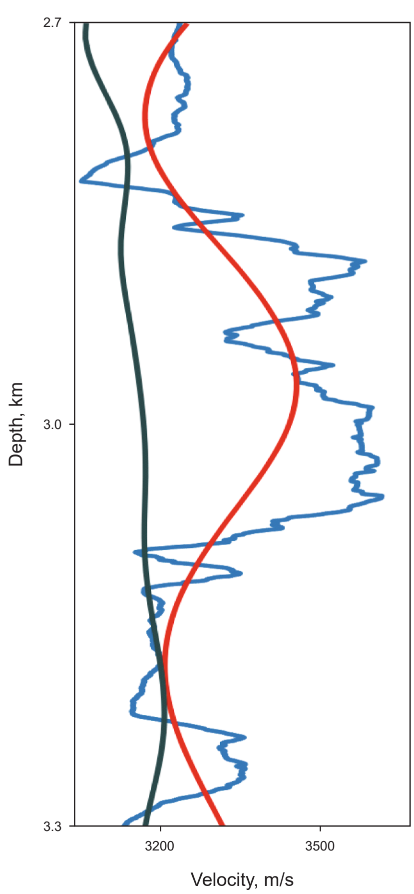

Fig. 10. Velocity comparison of well logging velocity (blue), initial velocity model (green) and FWI inverted velocity model (red).

The comparison of the inversion velocity model and the well log velocity proved that FWI can obtain more accurate subsurface velocity than the traditional method. Furthermore, the velocity model obtained from FWI accurately reflects the subsurface acoustic properties, which can also reveal some of the physical properties of the subsurface media. However, the identification of the boundary structures of the high-velocity anomalies is limited by the resolution of the velocity model, because only low-frequency information is used in the inversion. The PSDM image can provide subsurface structure information, but the fidelity of subsurface structure is contingent upon the accuracy of the velocity used in the migration process. The previous quality control process has proven that the velocity models obtained from FWI have higher accuracy, which makes the PSDM image more precise in revealing the subsurface structure. Therefore, by combining the velocity model with the migration image, its structural and lithological parameters can be obtained simultaneously, which helps analyze the possible location of oil and gas reservoirs in subsequent reservoir interpretation.

Fig. 11 shows the velocity and PSDM result using FWI inverted model in the high-velocity anomalies area. A positive reflection coefficient layer can be seen on both migration images, marked with red in Fig. 11(b) and (c). The positions of high-velocity anomalies are also marked in the PSDM image and velocity models. In the FWI results, the high-velocity area at this location is revealed, and the structure corresponds well to the layer structure in the migration image. High-velocity anomalies are one of the possible characteristics of oil or gas reservoirs. The depth of this area is consistent with the Liushagang 2 formation (L2 formation) in Wei Xi'nan Sag. The L2 group is mainly composed of source rocks and is a potential oil and gas layer (Liu et al., 2008; Xu and Wang, 2012; Xu et al., 2021). Since the high-velocity anomalies in the L2 group are located near the fault zone, it is inferred that this area is valuable for further analysis and exploration. The good correspondence between subsurface velocity and layer structure further proves the reliability of FWI. Also, it proves that FWI can not only provide a better migration velocity model but also be used to reveal areas with high value for oil and gas interpretation.

Although the location of high-velocity anomalies has been revealed by FWI, further analysis is required to infer its specific properties, such as AVA analysis. AVA (amplitude versus angle) analysis is a method that discerns the properties of subsurface materials by detecting variations in seismic wave amplitude corresponding to different incident angles. After the area for AVA analysis is selected, the properties of the substance are ascertained by acquiring the curve depicting amplitude variations with respect to the incident angle and contrasting it with a standard reference curve. The amplitude versus angle curve (AVA curve) can be

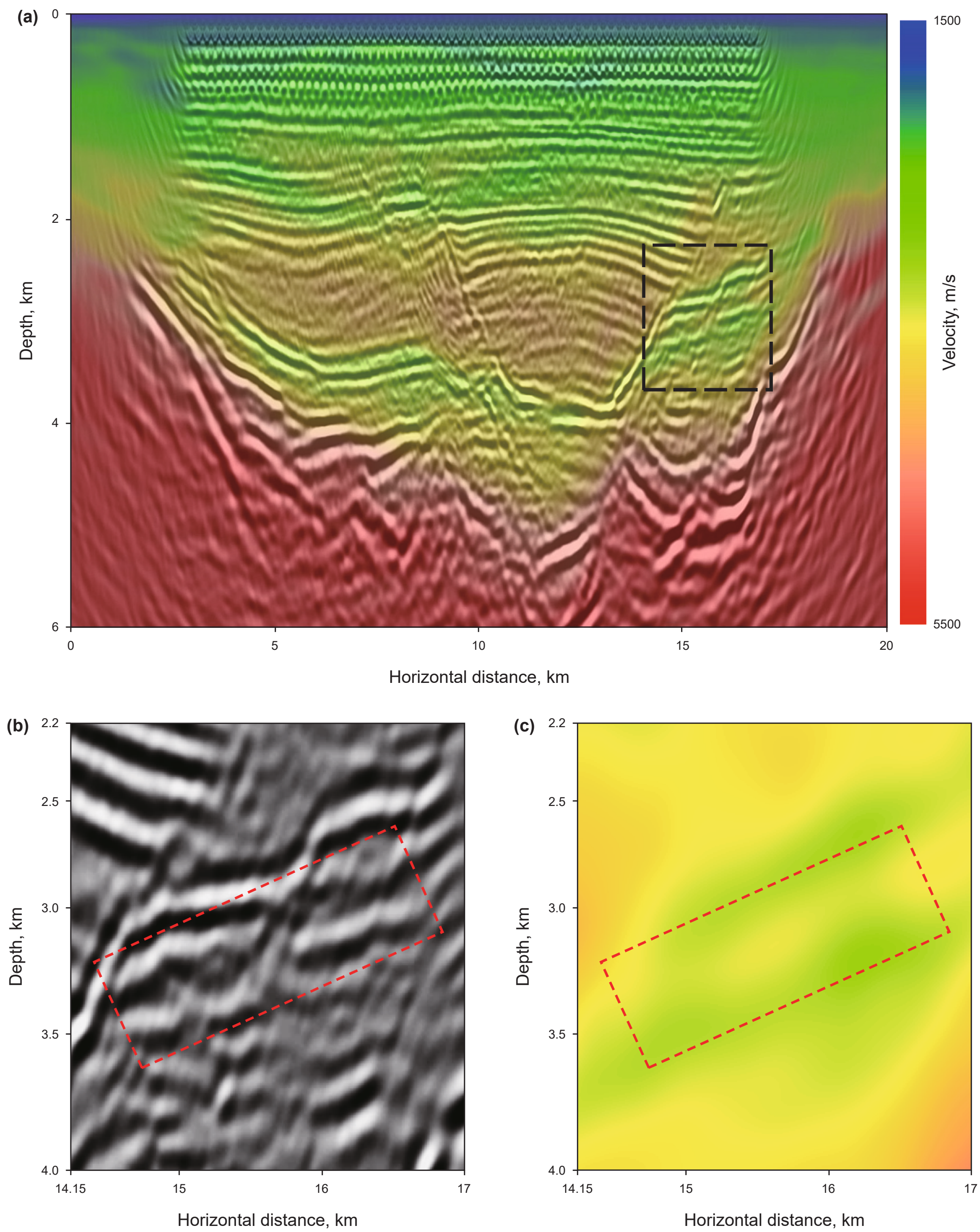

Fig. 11. Overlay of the PSDM image and FWI results. **(a)** Represents the overlay of PSDM image and FWI inverted model results, and the position of the high-velocity anomalies area is marked with black dotted box. **(b)** Represents the magnified PSDM image of the high-velocity anomalies area, and **(c)** represents the magnified FWI velocity model. The red box in (b) and (c) indicated the position of the high-velocity layer.

derived through various methods, one of which is using ADCIGs. Before analyzing the AVA curve, it is necessary to ensure that the reflection coefficients at different angles in the ADCIGs have the correct relative relationship. The ADCIGs are calculated from the RTM process, which can maintain the relative relationship between the amplitudes at different incident angles. Besides, the ADCIGs are obtained by using the Poynting vector (Zhang et al., 2023), which can maintain amplitude consistency and ensure that the AVA curve obtained correctly reflects the properties of the subsurface media.

Since the ADCIGs have been calculated in the previous analysis, the AVA curve of high-velocity anomalies is obtained and shown in Fig. 12(b) with a blue line and red cross, the location of the AVA curve is marked using a yellow line in Fig. 8. Standard AVA curves of four typical gas-bearing sandstones (Wang et al., 2017) are shown in Fig. 12(a). The AVA curve of Class I gas-bearing sandstone is also plotted in Fig. 12(b) with a red line. The comparison of Class I gas-bearing sandstone and potential reservoirs shows that the AVA curve of potential reservoirs and Class I sandstone exhibits similar trends. Class I gas-bearing sandstones are characterized by high impedance (Rutherford and Williams, 1989) and manifest as high-velocity anomalies in seismic velocity models, and concurrently, the FWI results present a high-velocity anomaly, suggestive of a possible Class I gas-bearing sandstone.

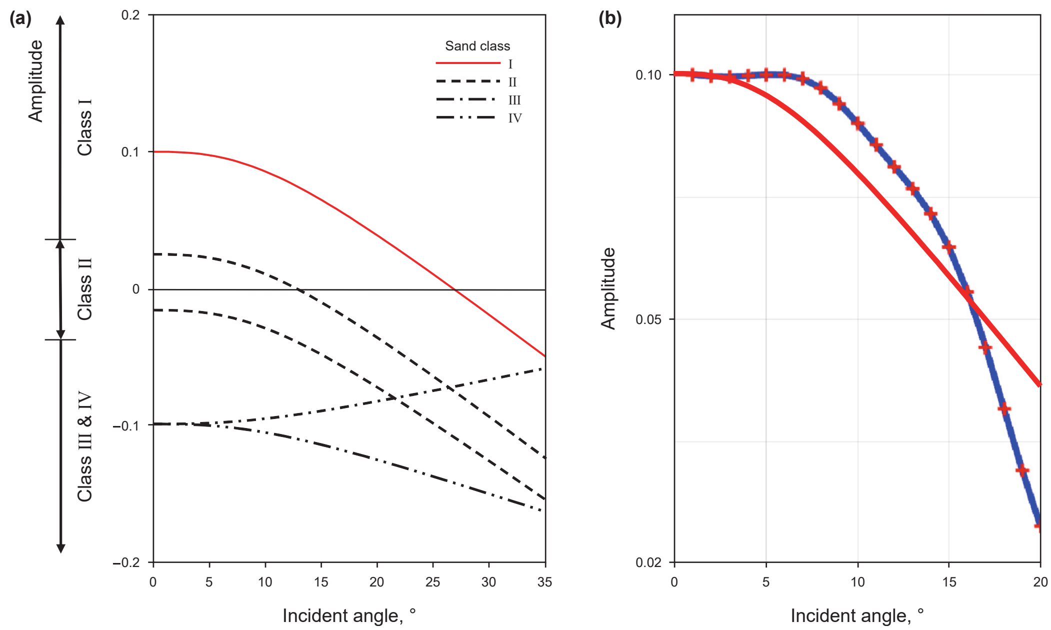

Fig. 12. (**a**) standard AVA curve of four classes sandstone (modified from Wang et al., 2017), (**b**) the AVA curve comparison of Class I sandstone and potential reservoir in field data. The AVA curve of Class I sandstone is represented with red line, the AVA curve calculated from the potential reservoir is represented with blue line and the amplitude calculated is marked with red cross.

4. Discussion

We have presented a 2D field data case study of complex fault imaging using full waveform inversion. The application of FWI to 2D dataset is affected by lateral reflections and diffractions, which complicates the 2D field data and makes it difficult to match the predicted data with the field data. Consequently, we employ the first arrival wave, excluding reflections, for inversion purposes and utilize a lower frequency band to mitigate the effects of lateral diffraction. Compared with traditional methods, FWI obtains a more accurate velocity model and some velocity anomalies are revealed based on FWI results and PSDM images. However, the resolution of FWI results is limited by the incomplete utilization of high-frequency information and the interpretation of these inverted velocity anomalies is still constrained by some limitations. For example, our FWI method is based on the acoustic wave equation, which can only reveal the acoustic property of subsurface media. Other important properties like elastic property are still lacking for oil and gas interpretation. It is hard to identify the material composition of the velocity anomalies from the velocity and PSDM images obtained by FWI, and further arguments are still needed. Using 3D data for FWI or utilizing the elastic wave FWI method to obtain the elastic properties of subsurface media will significantly enhance the effect of inversion, and provide more arguments for inferring the presence of oil and gas reservoirs.

After we obtained the FWI inverted result, many quality control methods are also used to detect whether the FWI operates correctly. The most direct and convenient quality control method is to compare the differences between modelled and observed data. This comparison can describe whether the FWI converges normally, but due to the nonlinearity of FWI, it cannot detect whether the velocity model is accurate. Another effective method is to compare whether the PSDM imaging accuracy is improved, which is also applied in our quality control (QC) process. We conducted a thorough analysis of the pre-stack depth migration images obtained using the inverted model. The results show that the PSDM image obtained by the inversion model has a higher resolution and better imaging effect at the fault location. This method can check whether the overall velocity model has been improved, but it cannot intuitively show the improvement of velocity details. Angle domain common imaging gathers (ADCIGs) is an effective tool for revealing velocity accuracy details (Zhang and Lu, 2022). Like CIG, ADCIGs will become flat when velocity is accurate, and the resolution of ADCIGs is higher than traditional CIG. The ADCIGs based on the migration results are compared to provide a more in-depth demonstration of the accuracy of the inversion results, and the ADCIGs at the fault location also prove the accuracy of the inversion model. The overlay of the inversion model and the migration results also confirmed that the velocity model obtained by FWI is more consistent with the subsurface geological structure, which also ensures the reliability of subsequent analysis. Through these comparisons, effective quality control of FWI can be carried out.

Moreover, more geological details are revealed by combining the PSDM image and FWI inverted velocity model. Unlike travel time tomography, which can only acquire background velocities, FWI provides a higher-resolution subsurface velocity model. Higher resolution velocity models can better correspond with the subsurface geological structures. In our study, the FWI inverted model shows good consistency with the structure of the PSDM images. Utilizing the physical property information provided by the velocity model and the structural information provided by the migration images allows for a preliminary interpretation of the subsurface stratigraphic attributes. High-velocity anomalies corresponding to the migration images were discovered in the FWI velocity model, with the surrounding background velocity being close to the average velocity of the source rocks in this area. These source rocks are considered the primary source of hydrocarbons, and the high-velocity anomalies may represent potential gas-bearing sandstone layers. Summarizing all the previous results and analyses, FWI results and ADCIGs images reveal that the inverted high-velocity anomalies area has the potential to be gas-bearing sandstone layer, but further analysis and arguments are still needed to identify its properties. This provides geologists with a reliable preliminary interpretation, thereby streamlining future research efforts. Through further analysis such as well logging chemical analysis, reservoir inversion and other analysis, the properties of these high-velocity anomalies can be confirmed, thereby accelerating the process of geological interpretation. These advantages of FWI are validated in this 2D OBC dataset.

5. Conclusion

In this paper, we applied the FWI method on 2D OBC data of fault area in the South China Sea, and obtained convincing PSDM image and ADCIGs. We also proved that the potential gas reservoirs can be revealed using FWI and AVA analysis. It should be noted that to achieve such effects, seismic data need to be processed specifically, and comprehensive quality control must be carried out to ensure the correct convergence of FWI. We processed the 2D OBC data with the primary goal of preserving low-frequency information while maximizing the signal-to-noise ratio, then finally obtained the FWI results and the corresponding migration image. There are fault structures beneath the survey area, and conventional velocity analysis methods make it hard to obtain high-resolution subsurface velocity results, presenting difficulties in using subsurface velocities to reveal material properties. The FWI results and the migration images have been proven to be of higher accuracy and have revealed potential gas-bearing reservoirs, which demonstrates the advantages of the FWI method in imaging and geological interpretation. It is important to note that our FWI method can only provide the location and acoustic velocity of potential hydrocarbon reservoirs, and the results still have uncertainty because it is limited by the resolution and the lack of other physical properties. Our intent in this paper is to present a possible application of full waveform inversion, the AVA analysis using FWI and ADCIGs is far from a true AVA inversion. But explorationists can use the analysis presented here as the first step in a more rigorous AVA analysis, because this analysis does not require additional computational cost and may accelerate the overall interpretation process.

CRediT authorship contribution statement

Kai Ren: Writing – review & editing, Writing – original draft, Visualization, Validation, Investigation, Data curation. **Shao-Ping Lu:** Writing – review & editing, Supervision, Funding acquisition, Conceptualization. **Xin-Tong Dong:** Data curation. **Xiang Li:** Software. **Xiao Ge:** Visualization, Methodology. **Shu-Kui Zhang:** Visualization, Methodology.

Declaration of competing interest

The authors declare that they have no known competing financial interests or personal relationships that could have appeared to influence the work reported in this paper.

Acknowledgements

This study is partially funded by the National Natural Science Foundation of China (Grant Nos. 42230805 and 42474137), the National Key Research and Development Program of China (Grant No. 2023YFF0803301).

References

Baysal, E., Kosloff, D.D., Sherwood, J.W.C., 1983. Reverse time migration. Geophysics 48 (11), 1514–1524. https://doi.org/10.1190/1.1441434.

Bording, R.P., Gersztenkorn, A., Lines, L.R., et al., 1987. Applications of seismic travel-time tomography. Geophys. J. Int. 90 (2), 285–303. https://doi.org/10.1111/j.1365-246X.1987.tb00728.x.

Borisov, D., Gao, F., Williamson, P., et al., 2020. Application of 2D full-waveform inversion on exploration land data. Geophysics 85 (2), R75–R86. https://doi.org/10.1190/geo2019-0082.1.

Brossier, R., Operto, S., Virieux, J., 2009. Seismic imaging of complex onshore structures by 2D elastic frequency-domain full-waveform inversion. Geophysics 74 (6), WCC105–WCC118. https://doi.org/10.1190/1.3215771.

Bunks, C., Saleck, F.M., Zaleski, S., et al., 1995. Multiscale seismic waveform inversion. Geophysics 60 (5), 1457–1473. https://doi.org/10.1190/1.1443880.

Buske, S., 1999. Three-dimensional pre-stack Kirchhoff migration of deep seismic reflection data. Geophys. J. Int. 137 (1), 243–260. https://doi.org/10.1046/j.1365-246x.1999.00789.x.

Cabrera, J., Perkins, W., Hagen, T., et al., 1992. 3-D prestack depth migration: Implementation and case history. Explor. Geophys. 23 (1–2), 43–46. https://doi.org/10.1071/EG992043.

Chauris, H., Noble, M.S., Lambaré, G., et al., 2002. Migration velocity analysis from locally coherent events in 2-D laterally heterogeneous media, Part II: Applications on synthetic and real data. Geophysics 67 (4), 1213–1234. https://doi.org/10.1190/1.1500383.

Davy, R.G., Morgan, J.V., Minshull, T.A., et al., 2018. Resolving the fine-scale velocity structure of continental hyperextension at the Deep Galicia Margin using full-waveform inversion. Geophys. J. Int. 212 (1), 244–263. https://doi.org/10.1093/gji/ggx415.

Deng, F., McMechan, G.A., 2007. True-amplitude prestack depth migration. Geophysics 72 (3), S155–S166. https://doi.org/10.1190/1.2714334.

Dickinson, D., Mancini, F., Li, X., et al.. A refraction/reflection full-waveform inversion case study from North West Shelf offshore Australia. https://doi.org/10.1190/segam2017-17404420.1.

Fei, W., McMechan, G.A., 2006. 3D common-reflection-point-based seismic migration velocity analysis. Geophysics 71 (5), S161–S167. https://doi.org/10.1190/1.2227523.

Gao, G., Xu, X., Liu, S., et al., 2020. Organic geochemistry identification of high-quality source rocks in the 2nd member of Liushagang Fm and its controls on petroleum occurrence in the Weixi'nan Sag,Beibuwan Basin. Oil Gas Geol. 41 (2), 339–347. https://doi.org/10.11743/ogg20200210 (in Chinese).

Gauthier, O., Virieux, J., Tarantola, A., 1986. Two-dimensional nonlinear inversion of seismic waveforms: numerical results. Geophysics 51 (7), 1387–1403. https://doi.org/10.1190/1.1442188.

Guitton, A., Valenciano, A., Bevc, D., et al., 2007. Smoothing imaging condition for shot-profile migration. Geophysics 72 (3), S149–S154. https://doi.org/10.1190/1.2712113.

Hu, W., Abubakar, A., Habashy, T.M., 2009. Simultaneous multifrequency inversion of full-waveform seismic data. Geophysics 74 (2), R1–R14. https://doi.org/10.1190/1.3073002.

Huang, R., Zhang, Z., Wu, Z., et al., 2021. Full-waveform inversion for full-wavefield imaging: decades in the making. Lead. Edge 40 (5), 324–334. https://doi.org/10.1190/tle40050324.1.

Jamali Hondori, E., Guo, C., Mikada, H., et al., 2021. Full-Waveform inversion for imaging faulted structures: A case study from the Japan Trench Forearc Slope. Pure Appl. Geophys. 178 (5), 1609–1630. https://doi.org/10.1007/s00024-021-02727-w.

Lee, K.H., Kim, H.J., 2003. Source-independent full-waveform inversion of seismic data. Geophysics 68 (6), 2010–2015. https://doi.org/10.1190/1.1635054.

Li, C.R., Zhang, G., Liang, J., et al., 2012. Characteristics of fault structure and its control on hydrocarbons in the Beibuwan Basin. Acta Pet. Sin. 33 (2), 195–203. https://doi.org/10.7623/syxb201202003.

Li, X., Esser, E., Herrmann, F.J., 2016. Modified Gauss-Newton full-waveform inversion explained—Why sparsity-promoting updates do matter. Geophysics 81 (3), R125–R138. https://doi.org/10.1190/geo2015-0266.1.

Li, X., Yao, G., Niu, F., et al., 2022. Waveform inversion of seismic first arrivals acquired on irregular surface. Geophysics 87 (3), R291–R304. https://doi.org/10.1190/geo2021-0097.1.

Liu, P., Xia, B., Zhang, Y., 2008. Fluid inclusions in reservoirs of Weixinan sag, Beibuwan Basin. Petroleum Exploration and Development 35 (2), 164–200. https://doi.org/10.1016/S1876-3804(08)60022-1.

Lu, S.P., 2021. Migration using sea surface-related multiples: Challenges and opportunities. Geophysics 86 (5), WC11–WC19. https://doi.org/10.1190/geo2020-0862.1.

McMechan, G.A., 1983. Migration by extrapolation of time-dependent boundary values. Geophysical Prospecting 31, 413–420. https://doi.org/10.1111/j.1365-2478.1983.tb01060.x.

Métivier, L., Allain, A., Brossier, R., et al., 2018. Optimal transport for mitigating cycle skipping in full-waveform inversion: A graph-space transform approach. Geophysics 83 (5), R515–R540. https://doi.org/10.1190/geo2017-0807.1.

Moczo, P., 1989. Finite-difference technique for SH-waves in 2-D media using irregular grids—Application to the seismic response problem. Geophys. J. Int. 99 (2), 321–329. https://doi.org/10.1111/j.1365-246X.1989.tb01691.x.

Mora, P., 1987. Nonlinear two-dimensional elastic inversion of multi-offset seismic data. Geophysics 52 (9), 1211–1228. https://doi.org/10.1190/1.1442384.

Nemeth, T., Wu, C., Schuster, G.T., 1999. Least-squares migration of incomplete reflection data. Geophysics 64 (1), 208–221. https://doi.org/10.1190/1.1444517.

Nocedal, J., Wright, S.J., 2006. In: Numerical Optimization, second ed. Springer.

Pladys, A., Brossier, R., Li, Y.B., Métivier, Ludovic, 2021. On cycle-skipping and misfit function modification for full-wave inversion: Comparison of five recent

approaches. Geophysics 86 (4), R563–R587. https://doi.org/10.1190/geo2020-0851.1.
Rutherford, S.R., Williams, R.H., 1989. Amplitude-versus-offset variations in gas sands. Geophysics 54 (6), P680–P688. https://doi.org/10.1190/1.1442696.
Sava, P.C., Fomel, S., 2003. Angle-domain common-image gathers by wavefield continuation methods. Geophysics 68 (3), 1065–1074. https://doi.org/10.1190/1.1581078.
Shin, C., Jang, S., Min, D., 2001. Improved amplitude preservation for prestack depth migration by inverse scattering theory. Geophys. Prospect. 49 (5), 592–606. https://doi.org/10.1046/j.1365-2478.2001.00279.x.
Sirgue, L., Barkved, O.I., Dellinger, J., et al., 2010. Thematic set: Full waveform inversion: the next leap forward in imaging at Valhall. First Break 28 (4). https://doi.org/10.3997/1365-2397.2010012.
Taillandier, C., Noble, M., Chauris, H., et al., 2009. First-arrival traveltime tomography based on the adjoint-state method. Geophysics 74 (6), WCB1–WCB10.
Tarantola, A., 1984. Inversion of seismic reflection data in the acoustic approximation. Geophysics 49 (8), 1259–1266. https://doi.org/10.1190/1.3250266.
Versteeg, R.J., 1993. Sensitivity of prestack depth migration to the velocity model. Geophysics 58 (6), 873–882. https://doi.org/10.1190/1.1443471.
Wang, X., Huang, J., Jiang, R., et al., 2017. AVO response of different types of gas-bearing sandstone and error analysis of approximate formulas. Litholog. Reserv. 29 (5), 120–126, 10/3969/j.issn.1673-8926.2017.05.014 (in Chinese).
Wang, J., Kuehl, H., Sacchi, M.D., 2005. High-resolution wave-equation AVA imaging: Algorithm and tests with a data set from the Western Canadian Sedimentary Basin. Geophysics 70 (5), S91–S99. https://doi.org/10.1190/1.2076748.
Wang, P., Zhang, Z., Mei, J., et al., 2019. Full-waveform inversion for salt: a coming of age. Lead. Edge 38 (3), 204–213. https://doi.org/10.1190/tle38030204.1.
Wang, Y., Zheng, Y.K., Zhang, L., et al., 2014. Reverse time migration of multiples: Eliminating migration artifacts in angle domain common image gathers. Geophysics 79 (6), S263–S270. https://doi.org/10.1190/geo2013-0441.1.
Warner, M., Guasch, L., 2016. Adaptive waveform inversion: Theory. Geophysics 81 (6), R429–R445. https://doi.org/10.1190/geo2015-0387.1.
Warner, M., Ratcliffe, A., Nangoo, T., et al., 2013. Anisotropic 3D full-waveform inversion. Geophysics 78 (2), R59–R80. https://doi.org/10.1190/geo2012-0338.1.
Xu, X., Wang, B., 2012. Oil sources of concealed reservoirs in Liushagang Formation of the Weixinan Sag and accumulation feature,Beibuwan Basin. Nat. Gas Geosci. 23 (1), 92–98 (in Chinese).
Xu, S., Wang, D., Chen, F., et al., 2012. Full waveform inversion for reflected seismic data. In: 74th EAGE Conference and Exhibition Incorporating EUROPEC 2012, cp-293-00729.. https://doi.org/10.3997/2214-4609.20148725.
Xu, J.J., Jin, Q., Xu, X.D., et al., 2021. Factors controlling organic-rich shale development in the Liushagang Formation, Weixinan Sag, Beibu Gulf Basin: Implications of structural activity and the depositional environment. Pet. Sci. 18 (4), 1011–1020. https://doi.org/10.1016/j.petsci.2020.08.001.
Yang, H.C., Zhang, J.Z., 2019. Full waveform inversion of combined towed streamer and limited OBS seismic data: A theoretical study. Mar. Geophys. Res. 40 (3), 237–244. https://doi.org/10.1007/s11001-018-9363-6.
Yang, H.C., Zhang, J.Z., Ren, K., et al., 2021. First-arrival traveltime inversion of seismic diving waves observed on undulant surface. Geophys. J. Int. 225 (2), 1020–1031. https://doi.org/10.1093/gji/ggab025.
Yoon, K., Marfurt, K.J., 2006. Reverse-time migration using the Poynting vector. Exploration Geophysics 37 (1), 102–107. https://doi.org/10.1071/EG06102.
Zhang, S.K., Lu, S.P., 2022. Residual moveout in angle gathers for converted waves. Geophysics 87 (3), U81–U92. https://doi.org/10.1190/geo2021-0366.1.
Zhang, Y., Zhang, G., Bleistein, N., 2005. Theory of true-amplitude one-way wave equations and true-amplitude common-shot migration. Geophysics 70 (4), E1–E10. https://doi.org/10.1190/1.1988182.
Zhang, S.K., Lu, S.P., Dong, X.T., et al., 2023. Angle-domain common-image gathers for imaging of multiples using poynting vectors. IEEE Trans. Geosci. Rem. Sens. 61, 1–13. https://doi.org/10.1109/TGRS.2023.3244574.
Zhang, S.K., Lu, S.P., Sacchi, M.D., 2024. Computing angle gathers from imaging of multiples using a Poynting vector method for improving angular illumination. IEEE Trans. Geosci. Rem. Sens. 62, 1–14. https://doi.org/10.1109/TGRS.2024.3384305.
Zhou, W., Brossier, R., Virieux, J., et al., 2016. Joint full-waveform inversion of early arrivals and reflections: A real OBC case study with gas cloud. In: SEG International Exposition and Annual Meeting, pp. 1247–1251. https://doi.org/10.1190/segam2016-13954099.1.
Zhou, X., Gao, G., Lü, X., et al., 2019. Petroleum source and accumulation of WZ12 oils in the Weixi'nan Sag, South China Sea, China. J. Petrol. Sci. Eng. 177, 681–698. https://doi.org/10.1016/j.petrol.2019.02.078.
Zhu, T., Cheadle, S., Petrella, A., et al., 2000. First-arrival tomography: Method and application. In: SEG Technical Program Expanded Abstracts 2000, pp. 2028–2031. https://doi.org/10.1190/1.1815839.